Molecular Control of the Nanoscale: Effect of Phosphine–Chalcogenide Reactivity on CdS–CdSe Nanocrystal Composition and Morphology

T. Purnima A. Ruberu,[†,‡] Haley R. Albright,[†,⊥] Brandon Callis,[‡,§] Brittney Ward,[‡,§] Joana Cisneros,[‡,§] Hua-Jun Fan,[‡,§] and Javier Vela[†,‡,*]

[†]Department of Chemistry, Iowa State University, Ames, Iowa 50011, United States, [‡]U.S. DOE Ames Laboratory, Ames, Iowa 50011, United States, and [§]Department of Chemistry, Prairie View A&M University, Prairie View, Texas 77446, United States. [⊥]Present address: University of Wisconsin, University Avenue, Madison, WI 53706.

ABSTRACT We demonstrate molecular control of nanoscale composition, alloying, and morphology (aspect ratio) in CdS–CdSe nanocrystal dots and rods by modulating the chemical reactivity of phosphine–chalcogenide precursors. Specific molecular precursors studied were sulfides and selenides of triphenylphosphite (TPP), diphenylpropylphosphine (DPP), tributylphosphine (TBP), trioctylphosphine (TOP), and hexaethylphosphorustriamide (HPT). Computational (DFT), NMR (^{31}P and ^{77}Se), and high-temperature crossover studies unambiguously confirm a chemical bonding interaction between phosphorus and chalcogen atoms in all precursors. Phosphine–chalcogenide precursor reactivity increases in the order: TPPE < DPPE < TBPE < TOPE < HPTE (E = S, Se). For a given phosphine, the selenide is always more reactive than the sulfide. $CdS_{1-x}Se_x$ quantum dots were synthesized *via* single injection of a R_3PS–R_3PSe mixture to cadmium oleate at 250 °C. X-ray diffraction (XRD), transmission electron microscopy (TEM), and UV/Vis and PL optical spectroscopy reveal that relative R_3PS and R_3PSe reactivity dictates $CdS_{1-x}Se_x$ dot chalcogen content and the extent of radial alloying (alloys *vs* core/shells). CdS, CdSe, and $CdS_{1-x}Se_x$ quantum rods were synthesized by injection of a single R_3PE (E = S or Se) precursor or a R_3PS–R_3PSe mixture to cadmium–phosphonate at 320 or 250 °C. XRD and TEM reveal that the length-to-diameter aspect ratio of CdS and CdSe nanorods is inversely proportional to R_3PE precursor reactivity. Purposely matching or mismatching R_3PS–R_3PSe precursor reactivity leads to $CdS_{1-x}Se_x$ nanorods without or with axial composition gradients, respectively. We expect these observations will lead to scalable and highly predictable "bottom-up" programmed syntheses of finely heterostructured nanomaterials with well-defined architectures and properties that are tailored for precise applications.

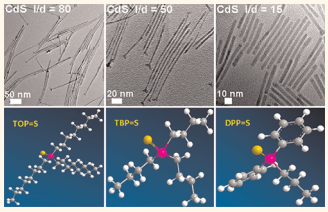

KEYWORDS: molecular control · precursor reactivity · nanocrystal composition · nanorod aspect ratio

Preparative nanotechnology or "nanomanufacturing" is rapidly evolving toward fabrication of ever more complex materials with precise structure and properties. Tuning composition, relative configuration, and spatial arrangement of heterostructured nanomaterials can impact our ability to engineer and direct energy flows at the nanoscale. In the case of II·VI and IV·VI semiconductors, composition control has been demonstrated for homogeneously alloyed $CdS_{1-x}Se_x$,[1–4] $CdS_{1-x}Te_x$,[5] $CdSe_{1-x}Te_x$,[6] PbS_xSe_{1-x}, PbS_xTe_{1-x}, and $PbSe_xTe_{1-x}$[7] nanocrystals with size- and composition-tunable band gaps.[4,8,9] In some cases, a nonlinear relationship between composition and absorption/emission energies, called optical bowing, resulted in new properties not obtainable from the parent binary systems.[3] For example, CdS_xTe_{1-x} nanocrystals displayed small absorption–emission spectral overlap, up to 150 nm Stokes shifts, and significantly red-shifted PL with respect to CdS and CdTe nanocrystals.[5]

Controlling nanocrystal morphology is key to controlling nanocrystal properties.[10–14] A common technique to produce nanorods, for example, is to perform slow and/or subsequent reactant injections.[15–17] In intrinsically anisotropic systems such as hexagonal (wurtzite) II·VI semiconductors, unidirectional (nanorod) growth occurs along the *c*(*z*) axis under high precursor concentrations. Bulky cadmium–phosphonate complexes are known to maintain high precursor concentrations *via* controlled release of Cd^{2+} ions to the medium.[18] Nearly spherical to rod-like shapes are produced using ligands such as hexyl phosphonic acid.[19] Aspect ratio is sensitive to phosphonic acid alkyl chain length; the shorter the chain, the more elongated and branched are the nanorods.[18,20] Aspect ratio control has been studied for ZnS, ZnSe,[16,21] ZnTe, CdS,[15] CdSe,[17–19] CdTe, $ZnS_{1-x-y}Se_xTe_y$, and $CdSe_{1-x}Te_x$[22] nanorods. ZnTe aspect ratio was controlled by temperature-tuning nanocrystal growth kinetics.[23] Composition-tunable CdSe, CdTe, and $CdSe_xTe_{1-x}$

* Address correspondence to vela@iastate.edu.

Received for review March 17, 2012 and accepted April 21, 2012.

Published online April 22, 2012
10.1021/nn301182h

tetrapods, the latter with nonlinear composition-dependent absorption and emission and spectral coverage up to 1000 nm (near-IR), were also reported.[22]

The mechanism by which cationic and phosphine−chalcogenide precursors react to form II·VI and IV·VI nanocrystals is currently under intense study and debate.[24,25] Two mechanisms, one involving Se^{2-} and another involving Se^0 transfer, were found to be simultaneously responsible for PbSe nanocrystal formation from $Pb(oleate)_2$ and phosphine selenides.[26] A kinetic model was used to describe combined nanocrystal nucleation and growth phenomena.[27] Reaction of $Pb(oleate)_2$ and trioctylphosphine selenide (TOPSe) at low temperature produced spherical PbSe nanocrystals, while reaction with hexaethylphosphorustriamide-triamide (HPT, also called tris(diethylamino)phosphine selenide) at high temperature produced PbSe nanorods. Coupled thermogravimetric mass spectrometry analysis (TGA-MS) showed that HPT accelerates precursor decomposition by releasing amines.[28]

Trioctyl- and tributylphosphine−chalcogenides (TOPE and TBPE; E = S, Se, Te) react with Cd and Zn oleates or alkylphosphonates *via* a Lewis acid substitution mechanism, producing ME (M = Cd, Zn) nanocrystals, phosphine oxides (TOPO or TBPO), and oleic or phosphonic anhydrides.[29] Using a high-throughput synthesis platform, CdSe yield as well as nucleation and growth rates from $Cd(ODPA)_2$ in TOPO were found to depend on phosphine selenide concentration and number of aryl groups.[30] Trialkylphosphine selenide P═Se bond cleavage starts by nucleophilic attack of carboxylate on Cd^{2+}-activated phosphine selenide, followed by proton transfer from carboxylic acid to Se and Cd−Se bond formation. The rate-limiting step lies at or before formation of acyloxytrialkylphosphonium ion, which was trapped with alcohols.[31] Reaction of DPPSe and $Cd(benzoate)_2$ in dodecylamine proceeds through a diphenyldiselenophosphinate intermediate and generates tetraphenyldiphosphine as a byproduct.[32] Magic-sized CdSe clusters are thought to be intermediates during CdSe nanorod synthesis from $Cd(phosphonate)_2$ and TOPSe in TOP−TOPO. Interestingly, acidic impurities accelerate reaction rates when technical grade rather than pure TOPO is used.[33] Tertiary phosphine selenide sources such as TOPSe were recently proposed to be unreactive toward metal carboxylates; small quantities of secondary phosphine impurities were proposed to be responsible for nanocrystal nucleation.[34] Whether this effect is catalytic or stoichiometric remains unknown.

In this paper, we use a combined experimental and theoretical approach to demonstrate that molecular precursor reactivity determines the relative ease of formation between nanocrystal phases. This opens new avenues for achieving predictable, molecular-level or "bottom-up" control of nanoscale composition and morphology. On the basis of our recent

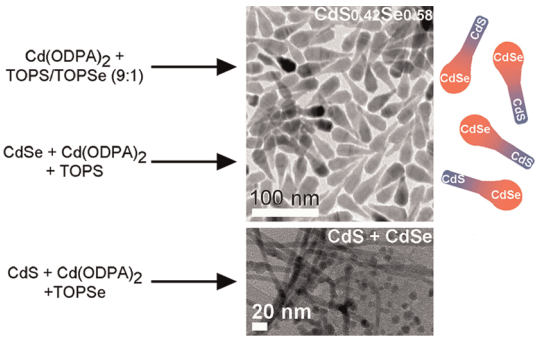

Scheme 1

observation of spontaneous formation of compositionally graded nanorods, this idea is consistent with Hammond's postulate, whereby the transition state energy for the rate-determining step, nucleation, is closest in energy to the precursors rather than to the much more stable nanocrystalline products, effectively a thermodynamic sink. We specifically focus on tuning sterics and electronics and therefore altering reactivity of different phosphine−chalcogenides (sulfides and selenides) in order to control architecture, composition, and aspect ratio of CdS−CdSe colloidal nanocrystals (dots and rods).

RESULTS AND DISCUSSION

Initial Observation: Spontaneous Formation of Composition-Graded, Axially Anisotropic $CdS_{1-x}Se_x$ Nanorods[35]. Using a single injection of premixed trioctylphosphine sulfur (TOPS) and trioctylphosphine selenium (TOPSe) to a bis(phosphonate)−cadmium $Cd(ODPA)_2$ complex at 320 °C, we recently synthesized axially anisotropic $CdS_{1-x}Se_x$ nanorods having a thick "head" and a thin "tail" (Scheme 1).[38] X-ray diffraction (XRD), high-resolution (HR) and energy-filtered (EF) transmission electron microscopy (TEM), and energy-dispersive X-ray spectroscopy (EDS) showed that nanorod heads are CdSe-rich, whereas nanorod tails are CdS-rich.[35] This axial anisotropy and composition gradient is accompanied by a marked band gap differential and allows directing metal (Pt, Pd) nanoparticle photodeposition toward either side of $CdS_{0.42}Se_{0.58}$ nanorods by changing irradiation wavelength.[36]

Time evolution and mechanistic studies showed that $CdS_{1-x}Se_x$ nanorods form sequentially, starting with quick CdSe head nucleation (<20 min), followed by slow CdS tail growth (~85 min) (Scheme 1). The relative ease of formation between these two nanorod segments cannot be a consequence of relative crystalline energies: CdS is much more stable (mp 1748 °C, lattice energy ~834 kcal/mol) compared to CdSe (mp 1512 °C, lattice energy ~798 kcal/mol).[35,37] Instead, this must be a consequence of relative TOPS *versus* TOPSe precursor reactivity. This idea is consistent with Hammond's postulate,[38] whereby *the transition state energy for the rate-determining step, nucleation,*

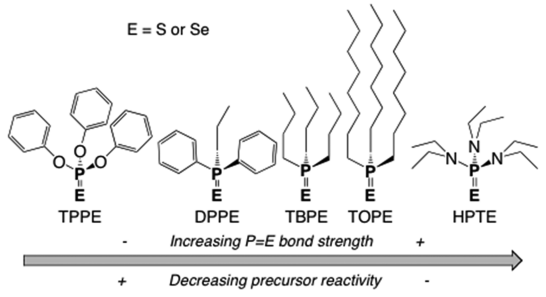

Figure 1. Phosphine–chalcogenide precursors used in this study.

is closest to the precursors than to the much more stable crystalline nanorods, effectively a thermodynamic sink.[39] If true, this could open new avenues for achieving molecular-level or "bottom-up" control of nanoscale composition and morphology. By tuning sterics and electronics and therefore altering molecular precursor reactivity, one could control relative formation rates of different nanocrystalline phases.

Here, we focused our attention on the reactivity of chalcogenide (sulfide and selenide) derivatives, $R_3P{=}E$, of five commercially available phosphines, R_3P: Triphenylphosphite (TPP), diphenylpropylphosphine (DPP), tributylphosphine (TBP), trioctylphosphine (TOP), and hexaethylphosphorustriamide (HPT) (Figure 1). All of the phosphines in this series are liquid at room temperature (RT), which facilitates precursor preparation by chemical "dissolution" of chalcogen (sulfur or selenium). On the contrary, triphenylphosphine, another commercially available phosphine, was not used here because it is a solid at RT (mp 79–81 °C). Qualitatively, we predicted that more electron-donating groups would lead to better stabilization of a partial positive charge on phosphorus, thus to stronger phosphorus–chalcogen (P=E) bonds and less reactive precursors (Figure 1).

Estimating Phosphine–Chalcogen Bond Strength and Relative Precursor Reactivity from DFT Calculations. To better understand these phenomena, we first turned our attention to computational modeling of the factors that control precursor reactivity at the atomic level. We focused on geometric and electronic properties around the reactive phosphorus–chalcogen bond. Table 1 lists relative energetic parameters, including zero-point energy correction (ΔE°_{ZPE}), enthalpies (ΔH°), and free energies (ΔG°) corrected to RT for the reaction $R_3P + S \rightarrow R_3PE$ (E = S or Se). In the optimized geometries, available in the Supporting Information, P=S bond lengths slightly increase from TPPS (1.921 Å) to DPPS (1.974 Å), TBPS (1.978 Å), TOPS (1.978 Å), and HPTS (1.982 Å). Similarly, P=Se bond lengths slightly increase from TPPSe (2.073 Å) to DPPSe (2.129 Å), TBPSe (2.131 Å), TOPSe (2.131 Å), and HPTSe (2.141 A). However, we do not believe this is an indication of relative P=E (S, Se) bond strength, but rather a

TABLE 1. Calculated Energy Parameters (kcal/mol) for Phosphine–Chalcogenide (R_3PS or R_3PSe) Formation

	ΔE°				ΔE°
basis set	6-311G*	ΔE°_{ZPE}	ΔH°	ΔG°	cc-pVTZ
Sulfides					
TPP + S → TPPS	−76.20	−74.06	−74.87	−64.66	−79.55
DPP + S → DPPS	−75.21	−73.35	−74.01	−63.91	−80.03
TBP + S → TBPS	−79.88	−77.71	−78.41	−68.38	−83.42
TOP + S → TOPS	−82.86	−80.99	−81.57	−71.60	−86.95
HPT + S → HPTS	−89.77	−86.71	−87.57	−77.60	−91.78
Selenides					
TPP + Se → TPPSe	−62.42	−60.84	−61.40	−51.67	−63.77
DPP + Se → DPPSe	−62.96	−61.63	−62.07	−52.10	−65.98
TBP + Se → TBPSe	−67.04	−65.43	−65.87	−56.23	−69.75
TOP + Se → TOPSe	−70.07	−68.60	−68.99	−59.10	−72.98
HPT + Se → HPTSe	−76.81	−74.38	−75.00	−65.22	−77.52

consequence of size and steric bulk of phosphorus substituents as reflected in the cone angles available for three phosphines in the series: TOP (128°), TBP (132°), DPP (136°).[40–43]

From Table 1, chalcogenide (E = S or Se) formation is exothermic or "downhill" ($\Delta G^\circ < 0$); that is, all phosphine–chalcogenides (R_3PE) are thermodynamically more stable than the reactants ($R_3P + E$). We believe the negative values $-\Delta G^\circ$ or $-\Delta E^\circ$ are good predictors of relative P=E bond strength and precursor reactivity. For example, calculated $-\Delta E^\circ$ values for trioctylphosphine (TOP) sulfide and selenide are ~87 and ~73 kcal/mol, respectively. These values roughly agree with previous results, which gave P=S and P=Se bond strengths of 96 and 75 kcal/mol, respectively.[44] The ΔE° difference between two phosphine–chalcogenides at the end of the series, TPPE and HPTE, is ~13 kcal/mol for S and ~14 kcal/mol for Se (solvation increases this difference to ~23 kcal/mol for S and ~16 kcal/mol for Se; see Supporting Information). Both $-\Delta G^\circ$ and $-\Delta E^\circ$ calculations clearly show phosphine–chalcogenide *stability relative to the release of free phosphine and chalcogen* increases in the order TPPE ~ DPPE < TBPE < TOPE < HPTE. Single-point energy ΔE° results using optimized geometries with 6-311G* and cc-pVTZ basis sets mirror this trend. Phosphine–chalcogenide precursor *reactivity*, understood as the *ability to give off or release chalcogen*, significantly decreases in the order TPPE ~ DPPE > TBPE > TOPE > HPTE (E = S, Se). This trend explains our aforementioned sequential formation of axially anisotropic $CdS_{1-x}Se_x$ nanorods: Because of significantly weaker P=E bond in TOPSe compared to TOPS (by 21 kcal/mol, Table 1), $Cd(ODPA)_2$ reacts faster with TOPSe than with TOPS, leading to faster CdSe nucleation compared to CdS.[35]

Figure 2 shows the highest occupied molecular orbital (HOMO) for HPTE and TPPE (E = S, Se). HOMOs are based on the one-node p-orbital interaction between P and E and are π-bond in character. The TPPSe

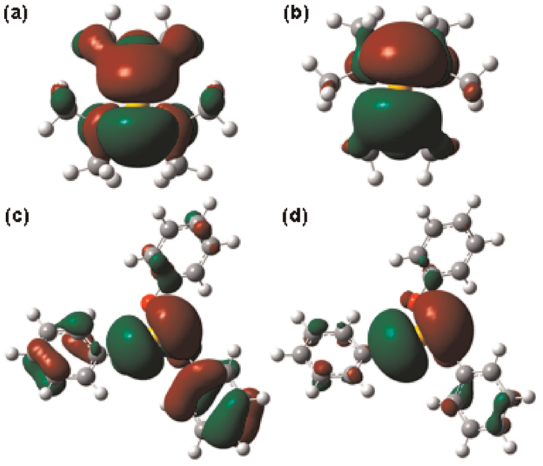

Figure 2. DFT-calculated highest occupied molecular orbitals (HOMOs) for HPTS (a), HPTSe (b), TPPS (c), and TPPSe (d) (viewed down the pseudo-$C_3(z)$ axis). The one-node π-interaction from the phenyl ring in TPPS is isolated from the P═S π-bond interaction.

HOMO has a small contribution from phenyl substituents, while the HPTS and HPTSe HOMOs have large amide nitrogen contributions. In TPPE, the oxygen between phenyl and P creates an electron density gap, and the oxygen lone pairs do not facilitate a π-interaction. In HPTE, the amine nitrogen directly connects to P, and the amide groups are situated perfectly for extensive π-interaction with P, making HPT bind S and Se very strongly. Much weaker π-interactions in TPP are observed in atomic polar tensor (APT) atomic populations analysis (unlike Mülliken analysis,[45−47] APT[48] analysis exhibits modest basis set sensitivity and models atomic populations more realistically).[49,50] Both analyses place positive and negative charges on P and E (S or Se), respectively. APT analysis shows a progressive increase of positive P charge upon going from free phosphine to phosphine−chalcogenide. Upon binding to E, APT P charge increases from TPP (0.622, S; 0.528, Se) to DPP (0.979, S; 0.872, Se), TBP (0.846, S; 0.750, Se), TOP (0.867, S; 0.767, Se), and HPT (0.866, S; 0.781, Se). Thus P polarization increases precursor stability; it is lowest for TPP, confirming TPPS and TPPSe as most reactive chalcogen sources in the series (Figure 1).

Estimating Phosphine−chalcogen Bond Strength and Reactivity from ^{31}P and ^{77}Se NMR. We used nuclear magnetic resonance (NMR) spectroscopy to gather experimental evidence that could substantiate these results. Specifically, we measured ^{31}P and ^{77}Se NMR spectra of the different phosphines, phosphine sulfide and phosphine selenide precursors (Table 2). Critically, ^{31}P resonances of all phosphine selenides (R_3PSe) show satellites characteristic of strong ^{31}P coupling (J = 330−520 Hz) to NMR active ^{77}Se (S = 1/2 nucleus with 7.58% natural abundance) (Figure 3a). Similarly, ^{77}Se resonances of all phosphine selenides (R_3PE) appear as doublets characteristic of strong ^{77}Se coupling to

TABLE 2. ^{31}P and ^{77}Se NMR Analysis of Phosphine−Chalcogenides[a]

	R_3P[b] ^{31}P δ/ppm	R_3PS[b] ^{31}P δ/ppm	R_3PSe[b] ^{31}P δ/ppm (J ^{31}P−^{77}Se/Hz)	R_3PSe[c] ^{77}Se δ/ppm (J ^{77}Se−^{31}P/Hz)
TPP	128.43 (s)	53.65 (s)	58.99 (s)[d] (513)	291.70 (d) (513)
DPP	−16.04 (s)	42.89 (s)	34.15 (s)[d] (360)	342.53 (d) (360)
TBP	−30.02 (s)	49.39 (s)	37.12 (s)[d] (339)	381.70 (d) (340)
TOP	−30.07 (s)	49.28 (s)	36.99 (s)[d] (339)	390.30 (d) (358)
HPT	122.58 (s)	82.37 (s)	82.21 (s)[d] (392)	258.78 (d) (386)

[a] s = singlet, d = doublet. [b] Referenced against 85% phosphoric acid, H_3PO_4 (δ 0 ppm). [c] Referenced against $PPh_3Se/CDCl_3$ (δ −266.20 ppm *vs* Me_2Se δ 0 ppm). [d] ^{77}Se satellites (7.58%) observed.

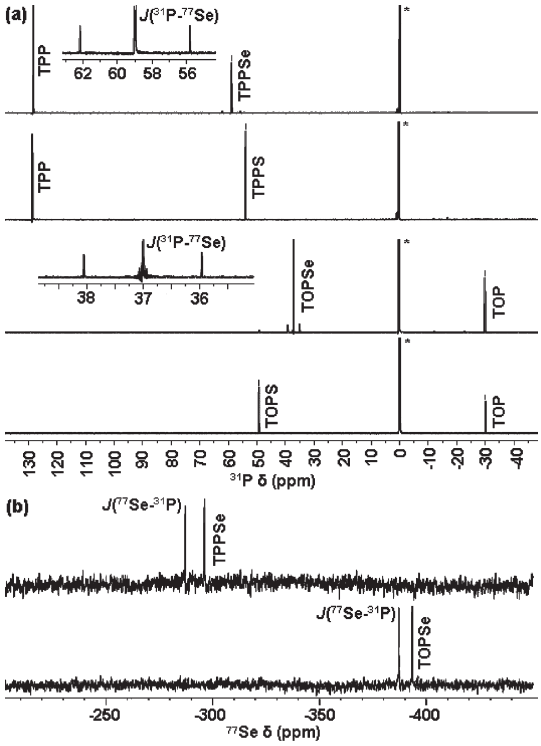

Figure 3. Sample (a) ^{31}P and (b) ^{77}Se NMR spectra of phosphine (R_3P) and phosphine−chalcogenide (R_3PE) precursors (E = S, Se). J(^{31}P−^{77}Se) coupling (330−520 Hz) is observed for R_3PSe by both ^{31}P and ^{77}Se NMR. * = 85% H_3PO_4 internal standard.

^{31}P (S = 1/2, 100% natural abundance) (Figure 3b). Observation of this coupling unambiguously corroborates the presence of phosphorus−selenium bonds in all selenide precursors; it also indirectly corroborates phosphorus−sulfur bonds in all sulfide precursors because P═S bonds are stronger than corresponding P═Se bonds (Table 1).[44]

Phosphine−chalcogenide (R_3P═Se, R_3P═S) ^{31}P NMR chemical shifts (δ) are more "downfield" (higher δ) compared to parent phosphines (R_3P), indicating that

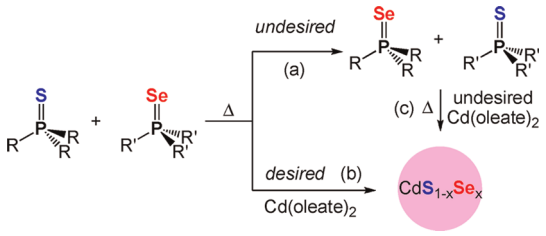

Scheme 2. High-temperature chalcogen exchange.

the P atom becomes more electron-deficient upon chalcogenide formation (HPT is the only exception; see Supporting Information). ^{31}P chemical shifts (δ) reflect relative P═E (S, Se) bond strengths; they correlate well with reported electron-donating abilities of phosphines, as reflected by available pK_a values: TOP (pK_a = 8.4), TBP (pK_a= 8.4), DPP (pK_a =4.9), and TPP (pK_a = 2.0) (TPP is the strongest base because its conjugate acid has the smallest pK_a).[51,52] ^{31}P NMR chemical shifts (δ) also correlate well with relative P═Se and P═S bond energies ($-\Delta G°$ values, Table 1) (HPT is again the exception; see below). Phosphine sulfide (R_3P═S) ^{31}P δ values are more downfield compared to phosphine selenide (R_3P═Se) δ values because S is smaller, more electronegative, and forms stronger P═E bonds than Se.

Minimizing Phosphine−Chalcogen Exchange: High-Temperature Crossover Experiments. We also probed the tendency of chalcogens to exchange or "crossover" between different phosphines (Scheme 2a). This question is important when two or more phosphine−chalcogenides are used as nanocrystal precursors (Scheme 2b,c); it also serves as an indirect test for the existence of P═S and P═Se bonds at high temperature. Specifically, we performed chalcogen crossover experiments between DPPS and TOPSe to give DPPSe and TOPS. According to Table 1, this exchange reaction is slightly exothermic (favorable), with a $\Delta G° = -0.69$ kcal/mol. Experimentally, we premixed DPPS and TOPSe at RT and injected this mixture to a Cd-free solution containing only oleic acid and dioctylamine under argon at different temperatures. Aliquots were drawn at different times, and the extent of chalcogen exchange was monitored by ^{31}P NMR. As shown in Figure 4, exchange at RT is very slow, with neither DPPSe nor TOPS being observed after 5 min. Exchange at very high temperature, such as 300 °C, is too fast, with as much as half of DPPS and TOPSe converted to DPPSe and TOPS after 5 min. Nevertheless, decreasing temperature somewhat and shortening reaction time helps minimize exchange. At 250 °C, the minimum temperature at which we see appreciable reaction between phosphine−chalcogenides and Cd(oleate)$_2$ or Cd(ODPA)$_2$ with immediate nuclei formation, DPPSe is unobserved and TOPS is a minor product after 0.5 min (Figure 4b).

Controlling $CdS_{1-x}Se_x$ Nanodot Composition. Having theoretical and experimental data at hand, we probed the effect of chalcogenide precursor reactivity on

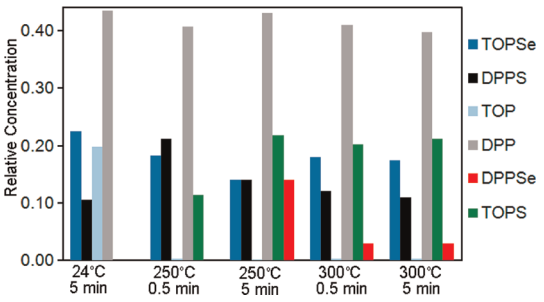

Figure 4. Chalcogen exchange between DPPS and TOPSe as a function of reaction temperature and time monitored by ^{31}P NMR.

TABLE 3. Controlling $CdS_{1-x}Se_x$ Nanodot Composition[a]

precursor mixture (ratio)[a]	$(-\Delta G°_{P=S}) - (-\Delta G°_{P=Se})$[b] (kcal/mol)	particle size (nm) XRD[c]	particle size (nm) TEM	band gap (eV)[d]	%S
TOPSe		2.2	4.6 ± 1.0	2.18	0
TOPS−TOPSe (3:1)	12.5	3.4	5.2 ± 0.9	2.13	1.8
DPPS−TOPSe (99:1)	4.81	3.2	4.8 ± 0.7	2.09	41
DPPS−TOPSe (199:1)	4.81	3.4	5.1 ± 0.9	2.12	54
TOPS		2.6	4.0 ± 0.6	2.80	100

[a] Phosphines premixed at RT before injection to Cd(oleate)$_2$ at 250 °C; dots grown 5 min at 250 °C. [b] Difference in $-\Delta G°$ values for chalcogenide formation estimated from Table 1. [c] From peak widths using the Scherrer equation. [d] Observed (apparent) band gap = $1240/\lambda_{1S}$.

nanocrystal composition by synthesizing $CdS_{1-x}Se_x$ nanodots using different phosphine sulfide (R_3PS) and phosphine selenide (R'_3PSe) combinations. According to Vegard's Law,[53] complete $CdS_{1-x}Se_x$ solid solutions are possible over a whole composition range ($0 \le x \le 1$). Both CdS and CdSe form zinc blende (cubic) and wurtzite (hexagonal) crystals, and four-coordinate S^{2-} and Se^{2-} ionic radii differ little, under <15% (4−7%).[54] Specific syntheses involved injecting fresh R_3PS−R'_3PSe mixtures to Cd(oleate)$_2$ at 250 °C and keeping the same (growth) temperature for 5 min. After isolation, we examined the resulting dots' optical properties, particle size (diameter), and composition using a combination of UV−Vis absorption and photoluminescence (PL) spectroscopies, XRD, TEM, and EDS (Table 3 and Figure 6).

XRD shows $CdS_{1-x}Se_x$ nanodots have cubic, zinc blende structures (Figure 5a). The *d* spacings extracted from XRD correlate well with chalcogenide (S:Se) composition obtained from EDS and chemical elemental analysis (%S, Figure 5b). DPPE, TBPE, and TOPE (E = S, Se) are reliable and useful chalcogen sources with varying reactivities. However, phosphines at the ends of the series in Figure 1, TPPE and HPTE, are too reactive and unreactive, respectively. TPPSe reacts with Cd(oleate)$_2$ too fast and forms aggregates rather than dots, whereas HPTS does not react at all. The P═Se bond in HPTSe is also very strong: According to XRD

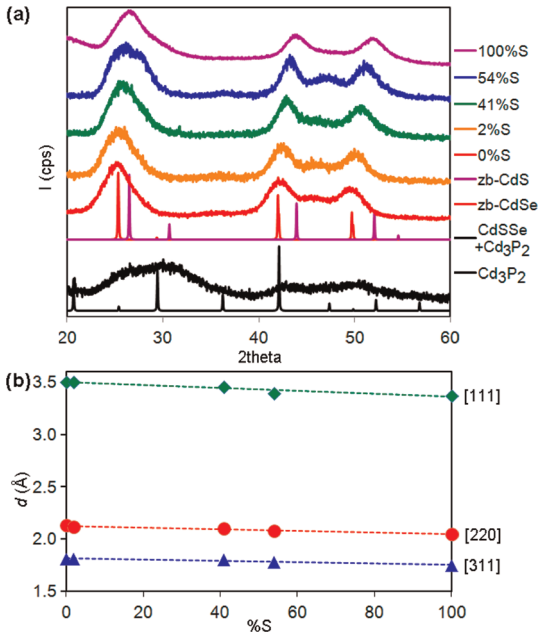

Figure 5. XRD patterns (a) and Vegard's plot (b) for $CdS_{1-x}Se_x$ dots obtained from different R_3PS-R_3PSe mixtures. In (a), reacting DPPS–HPTSe with $Cd(oleate)_2$ resulted in a mixture of CdSSe and Cd_3P_2.

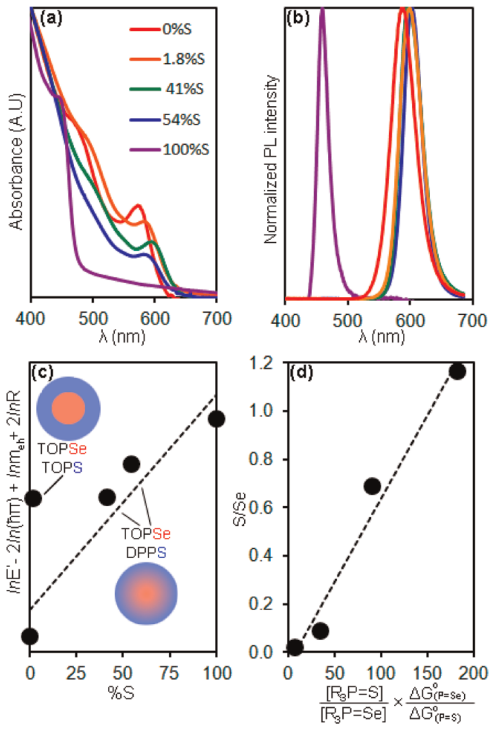

Figure 6. (a) UV–Vis, (b) PL, and (c) size-corrected band gaps of $CdS_{1-x}Se_x$ dots obtained from different R_3PS-R_3PSe mixtures. In (c), faster CdSe compared to CdS nucleation with TOPSe–TOPS leads to CdSe/CdS core/shells, whereas concomitant CdSe and CdS nucleation with TOPSe–DPPS leads to $CdS_{1-x}Se_x$ alloys. (d) Sulfur to selenium ratio (S/Se) in $CdS_{1-x}Se_x$ dots as a function of relative precursor concentration and reactivity: $\{([R_3PS]/[R_3PSe]) \times [(-\Delta G^\circ_{P=Se})/(-\Delta G^\circ_{P=S})]\}$. In (d), slope $k = 0.00688$.

and EDX, DPPS–HPTSe mixtures reacted with $Cd(oleate)_2$ to produce $CdS_{1-x}Se_x$ and Cd_3P_2 (Figure 5a).[28]

Observed nanodot band gaps appear erratic at first glance (Figure 6a,b); however, this is in great part due to different nanodot sizes across batches: Single-crystalline domain sizes (diameters) obtained from XRD peak widths are all smaller than Bohr radii for CdS (<3.0 nm) and CdSe (<5.6 nm) and are thus confined (quantized)[55] (Table 3). When corrected for size,[56] $CdS_{1-x}Se_x$ nanodot band gaps progressively widen (blue shift) with increasing sulfur content (Figure 6c). Critically, the band gap of nanocrystals made from sulfide and selenide precursors that are closer in reactivity, such as TOPSe–DPPS ($\Delta\Delta G^\circ_{P=E}$ = 4.81 kcal/mol), lie on or very near a straight line between the size-corrected band gaps of pure CdS and CdSe dots (Figure 6c). When two precursors have similar reactivity, they nucleate concomitantly at similar rates, forming true $CdS_{1-x}Se_x$ solid solutions. Solid solution band gaps are determined by the content-weighed band gap average between CdS and CdSe (Figure 6c). In contrast, the band gap of nanocrystals made from sulfide and selenide precursors with highly disparate reactivity, such as TOPSe–TOPS ($\Delta\Delta G^\circ_{P=E}$ = 12.5 kcal/mol), lie far from the straight line between the size-corrected band gaps for pure CdS and pure CdSe, a phenomenon known as "bowing" (Figure 6c).[3] When two precursors have very different reactivity, they nucleate separately at different rates (and times), forming CdSe/CdS core/shells. Core/shell band gaps are determined by CdSe core and degree of electron and hole delocalization into the CdS shell.[57–59] In other words, purposely matching or mismatching molecular precursor reactivity can control the degree of radial alloying and overall architecture of nanodots.

As reflected by XRD *d* spacings and size-corrected band gaps, nanodot elemental composition (EDS and elemental analysis) correlates well with relative phosphine–chalcogenide reactivity. Plotting (%S)/(%Se) content *versus* relative P═S and P═Se bond energies (estimated as the difference in $-\Delta G^\circ$ values from Table 1) shows %S increases and %Se decreases as the P═S bond becomes weaker and the P═Se bond becomes stronger (Figure 6c). We have used these data to develop an empirical expression that describes relative chalcogen content (S/Se) in $CdS_{1-x}Se_x$ nanodots as a function of theoretical and experimental parameters: The amount of each chalcogen incorporated should be (1) directly proportional to its precursor concentration (the more precursor molecules available, the more likely they will react with Cd), and (2) inversely proportional to its P═E bond energy (the stronger the bond, the more difficult it is to release chalcogen). Mathematically

$$S/Se \approx k \times ([R_3PS]/[R_3PSe]) \times [(-\Delta G^\circ_{P=Se})/(-\Delta G^\circ_{P=Se})]$$

where *k* is an empirically fitted dimensionless constant (Figure 6d).

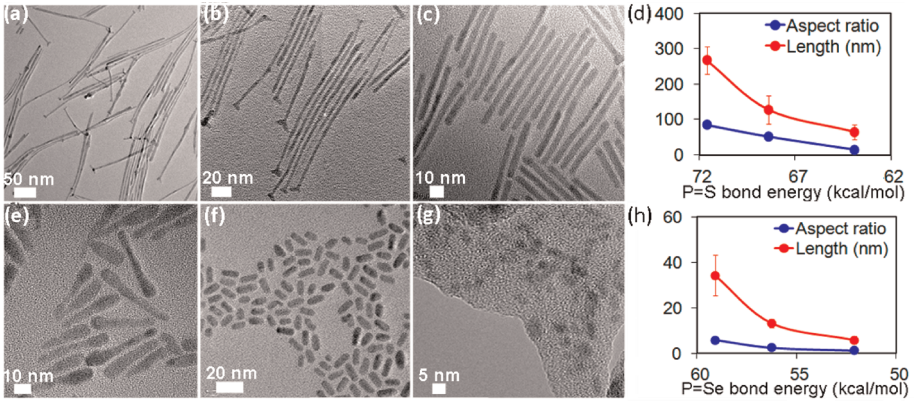

Figure 7. Change in nanorod aspect ratio as a function of precursor reactivity: CdS nanorods made with trioctylphosphine sulfide, TOPS (a), tributylphosphine sulfide, DPPS (b), and diphenylpropylphosphine sulfide, DPPS (c). Plot of CdS nanorod length (nm) and aspect ratio as a function of calculated P═S bond strength (energy in kcal/mol) (d). CdSe nanorods made with trioctylphosphine selenide, TOPSe (e), tributylphosphine selenide, TBPSe (f), and diphenylpropylphosphine selenide, DPPSe (g). Plot of CdSe nanorod length (nm) and aspect ratio as a function of calculated P═Se bond strength (energy in kcal/mol) (d). XRD shows all nanorods have mainly hexagonal (wurtzite) crystal structures.

TABLE 4. Controlling CdE Nanorod Aspect Ratio (E = S or Se)

entry	R_3PE	P═E energy[a] (kcal/mol)	length (nm)	diameter (nm)	aspect ratio (l/d)
		CdS nanorods[b]			
1	TOPS	71.60	267.0 ± 38.7	3.2 ± 0.6	83
2	TBPS	68.38	127.1 ± 2.5	2.5 ± 0.6	51
3	DPPS	63.91	64.4 ± 4.6	4.4 ± 1.1	15
		CdSe nanorods[c]			
4	TOPSe	59.10	34.3 ± 8.9	5.9 ± 1.1	6
5	TBPSe	56.23	13.2 ± 1.9	3.2 ± 1.9	2
6	DPPSe	52.10	5.9 ± 1.6	4.4 ± 1.4	1

[a] Estimated as $\Delta G°$ from Table 1. [b] Synthesized at 320 °C. [c] Synthesized at 250 °C.

Controlling CdE Nanorod Aspect Ratio (E = S or Se). We then moved our attention to the effect of phosphine–chalcogenide precursor reactivity on length-to-diameter "aspect ratio" of hexagonal (wurtzite) CdS and CdSe nanorods.[35] To probe this effect, we separately synthesized CdS and CdSe nanorods by single injection of one R_3PS or R_3PSe precursor, respectively, into a solution of $Cd(ODPA)_2$ at 320 °C for CdS or 250 °C for CdSe, and continued growth for 85 min. Lower reaction temperature was necessary for CdSe because phosphine selenides are less stable (more reactive) precursors compared to phosphine sulfides.[23] Figure 7 shows representative TEM images of CdS (a,b,c) and CdSe (e, f,g) nanorods obtained in this way. For both CdS and CdSe, nanorod length and aspect ratio consistently decrease as the phosphorus–chalcogen (P═E) bond energy decreases (Figure 7d,h and Table 4). In other words, nanorod length and aspect ratio decrease with increasing precursor reactivity.

We note the biggest contribution to observed changes in aspect ratio are nanorod lengths: CdS nanorod length changes from 267.0 ± 38.7 nm to 127.1 ± 2.5 nm and 64.4 ± 4.6 nm when TOPS, TBPS, and DPPS are used as sulfur precursors, respectively (Table 4, entries 1–3). CdSe nanorod length changes from 34.3 ± 8.9 nm to 13.2 ± 1.9 nm and 5.9 ± 1.6 nm when TOPSe, TBPSe, and DPPSe are used as selenium precursors, respectively (Table 4, entries 4–6). In contrast, changes in nanorod diameter are too small to be statistically significant: CdS nanorod diameters are 3.2 ± 0.6 nm, 2.5 ± 0.6 nm, and 4.4 ± 1.1 nm when TOPS, TBPS, and DPPS are used as sulfur precursors, respectively (Table 4, entries 1–3). CdSe nanorod diameters are 5.9 ± 1.1 nm, 3.2 ± 1.9 nm, and 4.4 ± 1.4 nm when TOPSe, TBPSe, and DPPSe are used as selenium precursors, respectively (Table 4, entries 4–6).

We rationalize these observations as follows: A decrease in phosphorus–chalcogen (P═E, E = S or Se) bond strength, that is, lower P═E bond energy, increases phosphine–chalcogenide precursor reactivity. More reactive R_3PE precursors react faster and more uncontrollably with $Cd(ODPA)_2$, leading to lower selectivity for anisotropic (unidirectional) 1D growth along wurtzite's *z*-axis and resulting in smaller nanorod aspect ratios. At the molecular level, we believe this is a nucleation-dominated effect: Each nanorod arises from a single initial nucleus or "seed" (small CdE cluster). Because nanorod diameters stay the same—within experimental error—for different precursors, we assume that they all grew from seeds formed at a similar, very early stage (*i.e.*, nucleation). Upon injection, more reactive precursors such as DPPS or DPPSe form many more nuclei compared to less reactive precursors such as TOPS or TOPSe. After this fast nucleation event, there is less of the more reactive precursor left in the reaction medium than of the less reactive precursor. This leads to more and shorter, lower aspect ratio nanorods for more reactive precursors than for less reactive (more stable) precursors.

TABLE 5. Controlling Axial Anisotropy and Composition Gradients along $CdS_{1-x}Se_x$ Nanorods[a]

precursor mixture (ratio)[a]	$(-\Delta G°_{P=S}) - (-\Delta G°_{P=Se})$[b]	length (nm)[c]	head diameter (nm)[c]	tail diameter (nm)[c]	aspect ratio[d]
TOPS—TOPSe (9:1)	12.5[a]	59.3 ± 8.0	17.8 ± 2.4	5.6 ± 0.8	3 to 11[e]
TBPS—TBPSe (9:1)	12.1[a]	13.2 ± 0.8	6.9 ± 0.8	6.9 ± 0.8	1.9

[a] Phosphines premixed at RT before injection to $Cd(ODPA)_2$ at 320 °C; rods grown 85 min. [b] Difference in $-\Delta G°$ values for chalcogenide formation estimated from Table 1. [c] From TEM. [d] Length/diameter. [e] Min/max.

The rate of chalcogen release from different molecular precursors *during growth* may also play a role in controlling nanorod aspect ratio. High precursor concentrations are known to favor unidirectional (1D) growth of wurtzite nanocrystals along the *z*-axis. A decrease in phosphorus—chalcogen bond strength accelerates the rate of chalcogen release to the reaction medium. More reactive precursors such as DPPS and DPPSe have weaker P═E bonds and cannot maintain high precursor concentrations for as long as less reactive precursors such as TOPS or TOPSe. Because high precursor concentrations are required for nanorod growth, more reactive precursors lead to shorter nanorods compared to less reactive (more stable) precursors.

The aforementioned trends also hold for analogous precursors across chalcogens (Table 4, entries 1—3 *vs* 4—6). Phosphine selenide precursors (R_3P═Se) have weaker phosphine—chalcogen bonds and are much more reactive than phosphine sulfide precursors (R_3P═S). As a result, CdSe nanorods form at lower temperatures (250 °C) compared to CdS nanorods (320 °C). Aspect ratio greatly decreases with increasing injection temperature: Only CdSe dots (l/*d* = 1) were formed at 320 °C.

Controlling $CdS_{1-x}Se_x$ Nanorod Axial Anisotropy and Composition Gradient. As mentioned above, we previously observed spontaneous formation of axially anisotropic $CdS_{0.42}Se_{0.58}$ nanorods by reacting a 9:1 TOPS—TOPSe mixture with $Cd(ODPA)_2$ at 320 °C for 85 min (Scheme 1); these graded nanorods have a length of 17.8 ± 2.4 nm and diameters of 17.8 ± 2.4 nm (CdSe "head") and 5.6 ± 0.8 nm (CdS "tail") (Table 5 and Figure 8a).[35] We explained the formation mechanism of these nanorods by considering relative TOPS and TOPSe reactivities. Our calculations show that the P═E bond in TOPS is 12.5 kcal stronger (less reactive) than that in TOPSe. Because of this large energy difference, fast (<20 min) CdSe homogeneous nucleation followed by slow (~85 min) CdS heterogeneous nucleation (epitaxial growth) along the nanorods *z*-axis leads to axially anisotropic rods (Figure 8a,c,e).

In contrast, we have observed formation of more regularly shaped $CdS_{0.34}Se_{0.66}$ nanorods by reacting a 9:1 TBPS—TBPSe mixture with $Cd(ODPA)_2$ at 320 °C for 85 min; these nanorods have a length of 13.2 ± 0.8 nm and a consistent diameter of 6.9 ± 0.8 nm (Table 5 and Figure 8b). The overall aspect ratio (1.9) is smaller compared to the aspect ratio of the axially anisotropic nanorods (3 to 7) (Table 5). Critically, EDS line scans show no composition gradient along the nanorods' length. We explain this uniform composition and consistent diameter (lack of axial anisotropy) based on relative TBPS and TBPSe reactivities. Our calculations show that the P═E bond in TBPS is somewhat closer in energy (12.1 kcal stronger less reactive than) compared to TOPSe. Because of this smaller energy difference, nanorods form by concomitant nucleation and growth of $CdS_{1-x}Se_x$ along the nanorods *z*-axis. As shown above for pure CdS and CdSe binary nanorods, overall aspect ratio is determined by relative precursor bond energies (and reactivities) in each case. The weighed averaged P═E bond energy ($-\Delta G_{ave}°$) for a 9:1 TOPS—TOPSe mix is 70.4 kcal/mol, whereas that for a 9:1 TBPS—TBPSe mix is 67.2 kcal/mol. As a result, axially anisotropic $CdS_{0.42}Se_{0.58}$ nanorods obtained with TOPS—TOPSe have a significantly higher aspect ratio (l/*d* up to 11) compared to regular $CdS_{0.34}Se_{0.66}$ nanorods obtained with TBPS—TBPSe (l/*d* = 1.9).

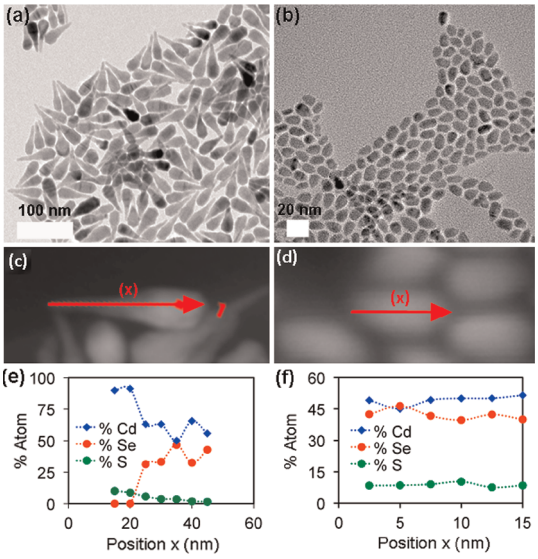

Figure 8. TEM images (a,b) and EDS line scans (c—f) of axially anisotropic $CdS_{0.42}Se_{0.58}$ nanorods made with a 9:1 TOPS—TOPSe precursor mixture (a,c,e) and regular $CdS_{0.34}Se_{0.66}$ nanorods made with a 9:1 TBPS—TBPSe precursor mixture (b,d,f). Arrows represent 50 nm in (c) and 17.5 nm in (d). Other conditions: $Cd(ODPA)_2$, 320 °C, 85 min. XRD shows that all nanorods have mainly hexagonal (wurtzite) crystal structures.

CONCLUSION

In summary, we have demonstrated predictable, "bottom-up" control of nanoscale composition, architecture, and morphology (aspect ratio) in CdS—CdSe nanocrystal quantum dots and rods by purposely altering and modulating the chemical reactivity of molecular phosphine—chalcogenide precursors, R_3PE

(E = S, Se). Computational (DFT), NMR (^{31}P and ^{77}Se), and high-temperature crossover studies unambiguously confirmed a chemical bonding interaction between phosphorus and chalcogen atoms in all R_3PE precursors. These studies showed phosphine−chalcogenide reactivity increases in the order TPPE < DPPE < TBPE < TOPE < HPTE (E = Se < Se). Structural (XRD, TEM, EDS) and optical (UV−Vis, PL) characterization of $CdS_{1-x}Se_x$ nanodots, synthesized by a single high-temperature injection of a R_3PS−R_3PSe mixture to cadmium oleate, reveals their elemental composition and degree of radial alloying depends on relative R_3PS and R_3PSe reactivity. Similarly, structural (XRD, TEM, EDS) characterization of CdS, CdSe, and $CdS_{1-x}Se_x$ nanorods, synthesized by high-temperature injection of individual R_3PE (E = S or Se) or R_3PS−R_3PSe precursor mixtures to cadmium phosphonate, reveals their length-to-diameter (aspect) ratio and a degree of axial alloying (composition gradient) depends on R_3PE precursor reactivity. We expect that these observations will contribute to the development of more predictable, bottom-up synthetic routes to fabricate well-defined heterostructures with highly specific properties. We are currently exploring this idea in the fabrication of nanomaterials for catalytic and thermoelectric applications.

METHODS

Materials. Cadmium oxide (99.998%), sulfur (99.999%), oleic acid (tech., 90%), and diphenylpropyl phosphine (DPP) (97%) were purchased from AlfaAesar; octadecylphosphonic acid (ODPA) from PCI synthesis; selenium (99.999%), trioctylphosphine oxide (TOPO) (99%), anhydrous toluene, hexaethylphosphoroustriamide (HPT) (97%), and dioctylamine (98%) from Sigma-Aldrich; triphenylphosphite (TPP) (97%), tributylphosphine (TBP) (99%), and trioctylphosphine (TOP) (97%) from Strem. Materials were used as received unless specified otherwise. NMR data were collected on either a Varian 400-MR or Varian VXR-400 spectrometer. ^{31}P NMR spectra were referenced to 85% phosphoric acid, H_3PO_4 (δ 0 ppm). ^{77}Se NMR spectra were referenced to $PPh_3Se/CDCl_3$ (δ −266.20 ppm *vs* Me_2Se δ 0 ppm).[60,61] Standards were sealed within capillaries in NMR tubes. Chemical elemental analyses were performed by Galbraith Laboratories., Inc. (Knoxville, TN).

Synthesis. *$CdS_{1-x}Se_x$ Nanodots.* R_3PS and R_3PSe stock solutions were made by dissolving 12.5 mmol of chalcogen (0.40 g of S or 0.98 g of Se) in 25 mmol phosphine (7.7 g of TPP, 5.7 g of DPP, 5.1 g of TBP, 9.3 g of TOP, or 6.2 g of HPT) in a dry-N_2-filled glovebox. *Synthesis*. CdO (24 mg, 0.18 mmol), OA (0.24 g, 0.85 mmol), and dioctylamine (8 g, 0.937 mmol) were heated to 100 °C, evacuated under dynamic vacuum for 15 min, refilled with argon, and heated to 300 °C to form a completely colorless solution. Solution was allowed to cool to 120 °C, evacuated under dynamic vacuum for 15 min, refilled with argon, and heated back to 250 °C. At 250 °C, a premixed R_3PS−R_3PSe (1 mL total volume, 1.14 mmol total chalcogens) was swiftly injected, causing a rapid color change. Mixture was stirred for 0.5 or 5 min at 250 °C, allowed to cool to RT, and diluted with toluene (5 mL). Nanocrystals were isolated by addition of methanol (24 mL), followed by centrifugation (5000 rpm for 10 min). *Chalcogen crossover control experiments*. TOPS (1.14 M, 0.3 mL) and DPPSe (1.14 M, 0.3 mL) were added to an NMR tube inside a dry-N_2-filled glovebox. The tube was sealed, and ^{31}P NMR was recorded RT as well as after heating to 100, 200, and 300 °C.

CdS Nanorods. CdS nanorods were made by a modified literature procedure.[35,62] R_3PS stock solutions were made by dissolving S (0.40 g, 12.5 mmol) in 12.5 mmol phosphine (2.9 g of DPP, 2.5 g of TBP, or 4.6 g of TOP) in a dry-N_2-filled glovebox. *Synthesis*. CdO (105 mg, 0.81 mmol), TOPO (1.3 g, 3.6 mmol), and ODPA (530 mg, 0.94 mmol) were heated to 100 °C, evacuated under dynamic vacuum for 15 min, refilled with argon, and heated to 320 °C to form a completely colorless solution. Solution was cooled to 120 °C, evacuated under dynamic vacuum for 15 min, refilled with argon, and heated back to 320 °C. When temperature reached 300 °C, phosphine (1.20 mL of DPP, TBP, or TOP) was injected into the flask. When temperature reached 320 °C, R_3PS stock solution (1 mL, 2.25 mmol DPPS, TBPS, or TOPS) was swiftly injected, causing a gradual color change. Temperature was equilibrated at 315 °C and stirring continued for 85 min. Final mixture was allowed to cool to R.T. and diluted with toluene (5 mL). Nanocrystals were isolated by addition of 1:1 v/v 2-propanol/nonanoic acid mixture (24 mL), followed by centrifugation (5000 rpm for 10 min). *CdSe nanorods*. R_3PSe stock solutions were made by dissolving Se (0.98 g, 12.5 mmol) in 12.5 mmol phosphine (2.9 g of DPP, 2.5 g of TBP, or 4.6 g of TOP) in a dry-N_2-filled glovebox. *Synthesis*. CdSe nanorods were made by a similar procedure as reported above for CdS nanorods, except that injection and growth were performed at 250 °C.

$CdS_{1-x}Se_x$ Nanorods. R_3PS and R_3PSe stock solutions were made as reported above for CdS and CdSe nanorods. Axially anisotropic $CdS_{0.42}Se_{0.58}$ nanorods with a "drumstick"-like morphology were synthesized by a literature procedure.[35] Regular (axially isotropic) $CdS_{0.34}Se_{0.66}$ nanorods were made as follows: CdO (105 mg, 0.81 mmol), TOPO (1.38 g, 3.6 mmol), and ODPA (540 mg, 0.94 mmol) were heated to 100 °C, evacuated under dynamic vacuum for 15 min, refilled with argon, and heated to 320 °C to form a completely colorless solution. Solution was cooled to 120 °C, evacuated under dynamic vacuum for 15 min, refilled with argon, and heated back to 320 °C. When temperature reached 300 °C, TBP (1.20 mL) was injected into the flask. When temperature reached 320 °C, a premixed, 9:1 TBPS−TBPSe solution (1 mL total volume, 2.25 mmol total chalcogens) was swiftly injected, causing a gradual color change. Temperature was equilibrated at 315 °C and stirring continued for 85 min. Final mixture was allowed to cool to RT and diluted with toluene (5 mL). Nanocrystals were isolated by addition of 1:1 v/v 2-propanol/nonanoic acid mixture (24 mL), followed by centrifugation (5000 rpm for 10 min).

Structural Characterization. *X-Ray Diffraction.* Powder X-ray diffraction (XRD) data were measured using Cu Kα radiation on a Scintag XDS-2000 diffractometer equipped with a theta−theta goniometer, a sealed-tube solid-state generator, and an air-cooled Kevex Psi Peltier silicon detector. *Transmission Electron Microscopy.* Transmission electron microscopy (TEM) was conducted on carbon-coated copper grids using a FEI Technai G2 F20 field emission scanning transmission electron microscope (STEM) at 200 kV (point-to-point resolution <0.25 nm, line-to-line resolution <0.10 nm). Nanorods' elemental axial composition was characterized by energy-dispersive spectroscopy (EDS) line scans in STEM mode and by energy-filtered (EF) imaging spectroscopy (EF-TEM). *Particle analysis.* Dimensions were measured manually and/or by using ImageJ. Size measurements and particle statistics were obtained for at least >100 $CdS_{1-x}Se_x$, CdS, and CdSe particles. Average sizes are reported along ± standard deviations.

Optical Characterization. Absorption spectra were measured with a photodiode array Agilent 8453 UV−Vis spectrophotometer. Solvent absorption was subtracted from all spectra. Steady-state photoluminescence (PL) spectra were measured with a Horiba-Jobin Yvon Nanolog scanning spectrofluorometer equipped with a photomultiplier detector. Photoluminescence (PL) quantum yields (QYs) were measured following

literature procedures.[63] Absorption and PL emission spectra were measured more than twice and average QYs recorded.

Computational Details. Calculations were carried out using the Gaussian 03 package[64] running on CenterOS based Linux cluster at the Prairie View A&M University. Tao-Perdew-Staroverov-Scuseria (TPSS) method,[65] a new generation of density functional implemented in Gaussian 03, was used for geometry optimization, solvation modeling, and frequency calculations. TPSS matches or exceeds in accuracy prior functionals, including the popular B3LYP with hybrid exchange functional.[66] TPSS recognizes relatively weak interactions such as agostic interactions, while B3LYP significantly underestimates them. Because hydrogen atoms in the modeled system do not play significant roles, a 6-311G* basis set[67,68] was used for all elements in our system. Not applying polarization functions on H's far away from P does not significantly degrade computational precision and accuracy and can considerably accelerate calculations.[69] All structures were fully optimized, and frequency analyses were performed until minima were achieved, with zero imaginary vibrational frequencies derived from vibrational frequency analysis. Thermodynamic functions including enthalpies, entropies, and free energies were calculated at 298.15 K and 1 atm. To examine basis set effects, a Dunning/Huzinaga full double-zeta[70] with Stuttgart/Dresden effective core potential basis set (SDD) and a triple-zeta Dunning's correlation consistent basis set (cc-pVTZ)[71] were used for all atoms with TPSS functionals to perform a single-point energy (SPE) calculation.

Conflict of Interest: The authors declare no competing financial interest.

Acknowledgment. This work is partially supported (1D semiconductor-based photocatalysts) by U.S. Department of Energy (DOE), Office of Basic Energy Sciences, Division of Chemical Sciences, Geosciences, and Biosciences through the Ames Laboratory. Ames Laboratory is operated for U.S. DOE by Iowa State University (ISU) under Contract No. DE-AC02-07CH11358. We thank ISU, Ames Lab Royalty Account, and Institute for Physical Research and Technology (IPRT) for startup funds (J.V.); Office of Science, U.S. DOE Visiting Faculty Program (VFP), and Faculty and Student Teams (FaST) for summer internships (B.C., B.W., J.C., and H.-J.F.); ISU Chemistry for a Hach Undergraduate Scholarship (H.R.A.); and Sarah Cady for ^{77}Se NMR assistance.

Supporting Information Available: Computational and additional experimental details including DFT-optimized geometries. This material is available free of charge *via* the Internet at http://pubs.acs.org.

REFERENCES AND NOTES

1. Swafford, L. A.; Weigand, L. A.; Bowers, M. J., II; McBride, J. R.; Rapaport, J. L.; Watt, T. L.; Dixit, S. K.; Feldman, L. C.; Rosenthal, S. J. Homogeneously Alloyed CdS_xSe_{1-x} Nanocrystals: Synthesis, Characterization, and Composition/Size-Dependent Band Gap. *J. Am. Chem. Soc.* **2006**, *128*, 12299–12306.
2. Ouyang, J.; Vincent, M.; Kingston, D.; Descours, P.; Boivineau, T.; Zaman, M. B.; Wu, X.; Yu, K. Noninjection, One-Pot Synthesis of Photoluminescent Colloidal Homogeneously Alloyed CdSeS Quantum Dots. *J. Phys. Chem. C* **2009**, *113*, 5193–5200.
3. Bailey, R. E.; Nie, S. M. Alloyed Semiconductor Quantum Dots: Tuning the Optical Properties without Changing the Particle Size. *J. Am. Chem. Soc.* **2003**, *125*, 7100–7106.
4. Regulacio, M. D.; Han, M.-Y. Composition-Tunable Alloyed Semiconductor Nanocrystals. *Acc. Chem. Res.* **2010**, *43*, 621–630.
5. Gurusinghe, N. P.; Hewa-Kasakarage, N. N.; Zamkov, M. Composition-Tunable Properties of CdS_xTe_{1-x} Alloy Nanocrystals. *J. Phys. Chem. C* **2008**, *112*, 12795–12800.
6. Wang, R.; Calvignanello, O.; Ratcliffe, C. I.; Wu, X.; Leek, D. M.; Zaman, M. B.; Kingston, D.; Ripmeester, J. A.; Yu, K. Homogeneously Alloyed CdTeSe Single-Sized Nanocrystals with Bandgap Photoluminescence. *J. Phys. Chem. C* **2009**, *113*, 3402–3408.
7. Smith, D. K.; Luther, J. M.; Semonin, O. E.; Nozik, A. J.; Beard, M. C. Tuning the Synthesis of Ternary Lead Chalcogenide Quantum Dots by Balancing Precursor Reactivity. *ACS Nano* **2011**, *5*, 183–190.
8. Jang, E.; Jun, S.; Pu, L. High Quality CdSeS Nanocrystals Synthesized by Facile Single Injection Process and Their Electroluminescence. *Chem. Commun.* **2003**, 2964–2965.
9. Smith, A. M.; Nie, S. Bright and Compact Alloyed Quantum Dots with Broadly Tunable Near-Infrared Absorption and Fluorescence Spectra through Mercury Cation Exchange. *J. Am. Chem. Soc.* **2011**, *133*, 24–26.
10. Peng, X. Mechanisms for the Shape-Control and Shape-Evolution of Colloidal Nanocrystals. *Adv. Mater.* **2003**, *15*, 459–463.
11. Manna, L.; Wang, L. W.; Cingolani, R.; Alivisatos, A. P. First-Principles Modeling of Unpassivated and Surfactant-Passivated Bulk Facets of Wurtzite CdSe: A Model System for Studying the Anisotropic Growth of CdSe Nanocrystals. *J. Phys. Chem. B* **2005**, *109*, 6183–6192.
12. Peng, X. A.; Peng, X. Mechanisms of the Shape Evolution of CdSe Nanocrystals. *J. Am. Chem. Soc.* **2001**, *123*, 1389–1395.
13. Talapin, D. V.; Shevchenko, E. V.; Murray, C. B.; Kornowski, A.; Förster, S.; Weller, H. CdSe and CdSe/CdS Nanorod Solids. *J. Am. Chem. Soc.* **2004**, *126*, 12984–12988.
14. Li, L.-S.; Alivisatos, A. P. Origin and Scaling of the Permanent Dipole Moment in CdSe Nanorods. *Phys. Rev. Lett.* **2003**, *90*, 097402-1–097402-4.
15. Saunders, A. E.; Ghezelbash, A.; Sood, P.; Korgel, B. A. Synthesis of High Aspect Ratio Quantum-Size CdS Nanorods and Their Surface-Dependent Photoluminescence. *Langmuir* **2008**, *24*, 9043–9049.
16. Cozzoli, P. D.; Manna, L.; Curri, M. L.; Kudera, S.; Gianninni, C.; Striccoli, M.; Agostiano, A. Shape and Phase Control of Colloidal ZnSe Nanocrystals. *Chem. Mater.* **2005**, *17*, 1296–1306.
17. Peng, Z. A.; Peng, X. Formation of High Quality CdTe, CdSe, and CdS Nanocrystals Using CdO as Precursor. *J. Am. Chem. Soc.* **2001**, *123*, 183–184.
18. Wang, W.; Banerjee, S.; Jia, S.; Steigerwald, M. L.; Herman, I. P. Ligand Control of Growth, Morphology, and Capping Structure of Colloidal CdSe Nanorods. *Chem. Mater.* **2007**, *19*, 2573–2580.
19. Peng, X.; Manna, L.; Yang, W.; Wickham, J.; Scher, E.; Kadavanich, A.; Alivisatos, P. Shape Control of CdSe Nanocrystals. *Nature* **2000**, *404*, 59–61.
20. Peng, Z. A.; Peng, X. Nearly Monodisperse and Shape-Controlled CdSe Nanocrystals *via* Alternative Routes: Nucleation and Growth. *J. Am. Chem. Soc.* **2002**, *124*, 3343–3353.
21. Panda, A. B.; Acharya, S.; Efrima, S.; Golan, Y. Synthesis, Assembly, and Optical Properties of Shape- and Phase-Controlled ZnSe Nanostructures. *Langmuir* **2007**, *23*, 765–770.
22. Li, Y.; Zhong, H.; Li, R.; Zhou, Y.; Yang, Z.; Li, Y. High-Yield Fabrication and Electrochemical Characterization of Tetrapodal CdSe, CdTe, and $CdSe_xTe_{1-x}$ Nanocrystals. *Adv. Funct. Mater.* **2006**, *16*, 1705–1716.
23. Zhang, J.; Jin, S.; Fry, H. C.; Peng, S.; Shevchenko, E.; Wiederrecht, G. P.; Rajh, T. Synthesis and Characterization of Wurtzite ZnTe Nanorods with Controllable Aspect Ratios. *J. Am. Chem. Soc.* **2011**, *133*, 15324–15327.
24. Bullen, C. R.; Mulvaney, P. Nucleation and Growth Kinetics of CdSe Nanocrystals in Octadecene. *Nano Lett.* **2004**, *4*, 2303–2307.
25. Yang, P.; Tretiak, S.; Ivanov, S. Influence of Surfactants and Charges on CdSe Quantum Dots. *J. Cluster Sci.* **2011**, *22*, 405–431.
26. Steckel, J. S.; Yen, B. K. H.; Oertal, D. C.; Bawendi, M. G. On the Mechanism of Lead Chalcogenide Nanocrystal Formation. *J. Am. Chem. Soc.* **2006**, *128*, 13032–13033.
27. Rempel, J. Y.; Bawendi, M. G.; Jensen, K. F. Insights into the Kinetics of Semiconductor Nanocrystal Nucleation and Growth. *J. Am. Chem. Soc.* **2009**, *131*, 4479–4489.

28. Koh, W.-K.; Yoon, Y.; Murray, C. B. Investigating the Phosphine Chemistry of Se Precursors for the Synthesis of PbSe Nanorods. *Chem. Mater.* **2011**, *23*, 1825–1829.
29. Liu, H.; Owen, J. S.; Alivisatos, A. P. Mechanistic Study of Precursor Evolution in Colloidal Group II–VI Semiconductor Nanocrystal Synthesis. *J. Am. Chem. Soc.* **2007**, *129*, 305–312.
30. Owen, J. S.; Chan, E. M.; Liu, H.; Alivisatos, A. P. Precursor Conversion Kinetics and the Nucleation of Cadmium Selenide Nanocrystals. *J. Am. Chem. Soc.* **2010**, *132*, 18206–18213.
31. García-Rodríguez, R.; Liu, H. Mechanistic Study of the Synthesis of CdSe Nanocrystals: Release of Selenium. *J. Am. Chem. Soc.* **2012**, *134*, 1400–1403.
32. Cossairt, B. M.; Owen, J. S. CdSe Clusters: At the Interface of Small Molecules and Quantum Dots. *Chem. Mater.* **2011**, *23*, 3114–3119.
33. Jiang, Z.-J.; Kelley, D. F. Role of Magic-Sized Clusters in the Synthesis of CdSe Nanorods. *ACS Nano* **2010**, *4*, 1561–1572.
34. Evans, C. M.; Evans, M. E.; Krauss, T. D. Mysteries of TOPSe Revealed: Insights into Quantum Dot Nucleation. *J. Am. Chem. Soc.* **2010**, *132*, 10973–10975.
35. Ruberu, T. P. A; Vela, J. Expanding the One-Dimensional CdS–CdSe Composition Landscape: Axially Anisotropic $CdS_{1-x}Se_x$ Nanorods. *ACS Nano* **2011**, *5*, 5775–5784.
36. Alemseghed, M. G.; Ruberu, T. P. A; Vela, J. Controlled Fabrication of Colloidal Semiconductor-Metal Hybrid Heterostructures: Site-Selective Metal Photo-deposition. *Chem. Mater.* **2011**, *23*, 3571–3579.
37. Xu, F.; Rock, P. A.; Ma, X.; Kauzlarich, S. M.; Navrotsky, A. Enthalpies of Formation of CdS_xSe_{1-x} Solid Solutions. *J. Mater. Res.* **2009**, *24*, 1368–1374.
38. Hammond, G. S. A Correlation of Reaction Rates. *J. Am. Chem. Soc.* **1955**, *77*, 334–338.
39. Bryan, J. D.; Gamelin, D. R. Doped Semiconductor Nanocrystals: Synthesis, Characterization, Physical Properties, and Applications. *Prog. Inorg. Chem.* **2005**, *54*, 47–126.
40. Chin, M.; Durst, G. L.; Head, S. R.; Bock, P. L.; Mosbo, J. A. Molecular Mechanics (MM2) Calculations and Cone Angles of Phosphine Ligands. *J. Organomet. Chem.* **1994**, *470*, 73–85.
41. Min, W. J.; Jung, S.; Lim, S. J.; Kim, Y.; Shin, S. K. Collision-Induced Dissociation of II–VI Semiconductor Nanocrystal Precursors, Cd^{2+} and Zn^{2+} Complexes with Trioctylphosphine Oxide, Sulfide, and Selenide. *J. Phys. Chem. A* **2009**, *113*, 9588–9594.
42. White, D.; Coville, N. J. Quantification of Steric Effects in Organometallic Chemistry. *Adv. Organomet. Chem.* **1994**, *36*, 95–158.
43. Brown, T. L.; Lee, K. J. Ligand Steric Properties. *Coord. Chem. Rev.* **1993**, *128*, 89–116.
44. McDonough, J. E.; Mendiratta, A.; Curley, J. J.; Fortman, G. C.; Fantasia, S.; Cummins, C. C.; Rybak-Akimova, E. V.; Nolan, S. P.; Hoff, C. D. Thermodynamic, Kinetic, and Computational Study of Heavier Chalcogen (S, Se, and Te) Terminal Multiple Bonds to Molybdenum, Carbon, and Phosphorus. *Inorg. Chem.* **2008**, *47*, 2133–2141.
45. Bachrach, S. M. In *Reviews in Computational Chemistry*; Lipkowitz, K. B., Boyd, D. B., Eds.; VCH: New York, 1995; Vol. V.
46. Mulliken, R. S. Electronic Structures of Polyatomic Molecules and Valence II. General Considerations. *Phys. Rev.* **1932**, *41*, 49–71.
47. Mulliken, R. S. Electronic Population Analysis on LCAO-MO Molecular-Wave Functions I–IV. *J. Chem. Phys.* **1955**, *23*, 1833–1840.
48. Cioslowski, J. A New Population Analysis Based on Atomic Polar Tensors. *J. Am. Chem. Soc.* **1989**, *111*, 8333–8336.
49. Amarasekara, A. S.; Lewis, D.; Nayani, S. L.; Timofeeva, T. V.; Fan, H.-J. X-ray Crystallography and Computational Studies of the Structure of Bis-nitrone, 2,5-Bis{[methyl(oxido)-imino]phenyl}furan. *J. Mol. Struct.* **2010**, *977*, 175–179.
50. Breneman, C. M.; Wiberg, K. B. Determining Atom-Centered Monopoles from Molecular Electrostatic Potentials. The Need for High Sampling Density in Formamide Conformational Analysis. *J. Comput. Chem.* **1990**, *11*, 361–373.
51. Bush, R. C.; Angelici, R. J. Phosphine Basicities As Determined by Enthalpies of Protonation. *Inorg. Chem.* **1988**, *27*, 681–686.
52. Henderson, W. A.; Streuli, C. A. The Basicity of Phosphines. *Anal. Chem.* **1960**, *32*, 985–987.
53. Denton, A. R.; Ashcroft, N. W. Vegard's Law. *Phys. Rev. A* **1991**, *43*, 3161–3164.
54. Shannon, R. D. Revised Effective Ionic Radii and Systematic Studies of Interatomic Distances in Halides and Chalcogenides. *Acta Crystallogr., Sect. A* **1976**, *32*, 751–767.
55. Zhong, X.; Feng, Y.; Knoll, W.; Han, M. Alloyed $Zn_xCd_{1-x}S$ Nanocrystals with Highly Narrow Luminescence Spectral Width. *J. Am. Chem. Soc.* **2003**, *125*, 13559–13563.
56. Hollingsworth, J. A.; Klimov, V. I. Soft Chemical Synthesis and Manipulation of Semiconductor Nanocrystals. In *Nanocrystal Quantum Dots*, 2nd ed.; Klimov, V. I., Ed.; CRC Press: Boca Raton, FL, 2010; pp 1–61.
57. Guo, Y.; Marchuk, K.; Sampat, S.; Abraham, R.; Fang, N.; Malko, A. V.; Vela, J. Unique Challenges Accompany Thick-Shell CdSe/*n*CdS ($n > 10$) Nanocrystal Synthesis. *J. Phys. Chem. C* **2012**, *116*, 2791–2800.
58. García-Santamaría, F.; Chen, Y. F.; Vela, J.; Schaller, R. D.; Hollingsworth, J. A.; Klimov, V. I. Suppressed Auger Recombination in Giant Nanocrystals Boosts Optical Gain Performance. *Nano Lett.* **2009**, *9*, 3482–3488.
59. Van Embden, J.; Jasieniak, J.; Mulvaney, P. Mapping the Optical Properties of CdSe/CdS Heterostructure Nanocrystals: The Effects of Core Size and Shell Thickness. *J. Am. Chem. Soc.* **2009**, *131*, 14299–14309.
60. Cullen, E. R.; Guziec, F. S.; Murphy, C. J.; Wong, T. C.; Andersen, K. K. Selenium-77 NMR Studies of Some Organoselenium Compounds Containing Carbon-Selenium Double Bonds. *J. Am. Chem. Soc.* **1981**, *103*, 7055–7057.
61. Bullen, C.; van Embden, J.; Jasieniak, J.; Cosgriff, J. E.; Mulder, R. J.; Rizzardo, E.; Gu, M.; Raston, C. L. High Activity Phosphine-Free Selenium Precursor Solution for Semiconductor Nanocrystal Growth. *Chem. Mater.* **2010**, *22*, 4135–4143.
62. Robinson, R. D.; Sadtler, B.; Demchenko, D. O.; Erdonmez, C. K.; Wang, L.-W.; Alivisatos, A. P. Spontaneous Superlattice Formation in Nanorods through Partial Cation Exchange. *Science* **2007**, *317*, 355–358.
63. Grabolle, M.; Spieles, M.; Lesnyak, V.; Gaponik, N.; Eychmüller, A.; Resch-Genger, U. Determination of the Fluorescence Quantum Yield of Quantum Dots: Suitable Procedures and Achievable Uncertainties. *Anal. Chem.* **2009**, *81*, 6285–6294.
64. Frisch, M. J.; Trucks, G. W.; Schlegel, H. B.; Scuseria, G. E.; Robb, M. A.; Cheeseman, J. R.; Montgomery, J. A.; Vreven, T.; Kudin, K. N.; Burant, J. C.; *et al. Gaussian 03*, revision D.01; Gaussian Inc.: Wallingford, CT, 2004.
65. Tao, J. M.; Perdew, J. P.; Staroverov, V. N.; Scuseria, G. E. Climbing the Density Functional Ladder: Nonempirical Meta-Generalized Gradient Approximation Designed for Molecules and Solids. *Phys. Rev. Lett.* **2003**, *91*, 12129–12137.
66. Staroverov, V. N.; Scuseria, G. E.; Tao, J. M.; Perdew, J. P. Comparative Assessment of a New Nonempirical Density Functional: Molecules and Hydrogen-Bonded Complexes. *J. Chem. Phys.* **2003**, *119*, 12129–12137.
67. Hehre, W. J.; Ditchfie, R; Pople, J. A. Self-Consistent Molecular-Orbital Methods 12. Further Extensions of Gaussian-Type Basis Sets for Use in Molecular-Orbital Studies of Organic Molecules. *J. Chem. Phys.* **1972**, *56*, 2257–2261.
68. Krishnan, R.; Binkley, J. S.; Seeger, R.; Pople, J. A. Self-Consistent Molecular-Orbital Methods 20. Basis Set for Correlated Wave Functions. *J. Chem. Phys.* **1980**, *72*, 650–654.
69. Fan, Y. B.; Hall, M. B. The Competition between Allene and Butadiene in the Carbon–Hydrogen Bond Activation Initiated by a Tungsten Allyl Complex: A DFT Study. *Organometallics* **2005**, *24*, 3827–3835.

70. Dunning, T. H.; Hay, P. J. In *Modern Theoretical Chemistry*; Schaefer, H. F., Ed.; Plenum: New York, 1976; Vol. 3, pp 1−28.
71. Kendall, R. A.; Dunning, T. H.; Harrison, R. J. Electron Affinities of the First-Row Atoms Revisited. Systematic Basis Sets and Wave Functions. *J. Chem. Phys.* **1992**, *96*, 6796–806.